Tracking the Cracking: a Holistic Analysis of Rapid Ice Shelf Fracture Using Seismology, Geodesy, and Satellite Imagery on the Pine Island Glacier Ice Shelf, West Antarctica

Seth Olinger[1], Bradley Paul Lipovsky[2], Marine Denolle[1], and Brendan W Crowell[2]

[1]Harvard University
[2]University of Washington

November 30, 2022

Abstract

Ice shelves regulate the stability of marine ice sheets. We track fractures on Pine Island Glacier (PIG) –a quickly accelerating glacier in West Antarctica that contributes more to sea level rise than any other glacier. TerraSAR-X imagery from 2012-2014 shows the formation of wing cracks, new rift formation, opening along a large rift, small calving events, and one large tabular calving event. Using a temporary on-ice seismic network, we catalog icequakes that dominantly consist of flexural gravity waves. The icequakes occur in three spatial groups: near the rift tip, where the rift reaches the margin, and the transition between intact and damaged margin. Rift tip icequakes correlate with ice speed and therefore link glaciological stresses and fracture. Using a simple flexural gravity wave model, we deconvolve wave propagation effects to estimate icequake source durations $O[10$ s$]$ and transient loads $O[$kPa$]$ corresponding to $ O[m]$ of crevasse growth per icequake.

Posted on 30 Nov 2022 — CC-BY-NC 4 — https://doi.org/10.1002/essoar.10510107/v1 — This a preprint and has not been peer reviewed. Data may be preliminary.

Tracking the Cracking: a Holistic Analysis of Rapid Ice Shelf Fracture Using Seismology, Geodesy, and Satellite Imagery on the Pine Island Glacier Ice Shelf, West Antarctica

S. D. Olinger[1,2], B. P. Lipovsky[2], M. A. Denolle[2], B. W. Crowell[2]

[1]Department of Earth and Planetary Sciences, Harvard University, Cambridge, Massachusetts, USA
[2]Department of Earth and Space Sciences, University of Washington, Seattle, Washington, USA

Key Points:

- Margin and rift fracture at PIG generate flexural gravity waves, a wave type related to interaction between a floating plate and supporting fluid.
- Relative event counts suggest that PIG's margin concentrates more stress than the rift tip, but only rift tip fracture seems related to ice speed.
- Recorded flexural gravity waves are consistent with a point moment or point load applied over ∼30 s, corresponding to ∼11 m of vertical cracking.

Corresponding author: Seth D. Olinger, `setholinger@fas.harvard.edu`

Abstract

Ice shelves regulate the stability of marine ice sheets. We track fractures on Pine Island Glacier (PIG) –a quickly accelerating glacier in West Antarctica that contributes more to sea level rise than any other glacier. TerraSAR-X imagery from 2012-2014 shows the formation of wing cracks, new rift formation, opening along a large rift, small calving events, and one large tabular calving event. Using a temporary on-ice seismic network, we catalog icequakes that dominantly consist of flexural gravity waves. The icequakes occur in three spatial groups: near the rift tip, where the rift reaches the margin, and the transition between intact and damaged margin. Rift tip icequakes correlate with ice speed and therefore link glaciological stresses and fracture. Using a simple flexural gravity wave model, we deconvolve wave propagation effects to estimate icequake source durations O[10 s] and transient loads O[kPa] corresponding to O[m] of crevasse growth per icequake.

1 Plain Language Summary

Large shelves of floating ice strengthen glaciers in Antarctica, helping to protect against rapid sea level rise that can occur when glaciers flow into the ocean. Ice shelves can collapse through rapid cracking (synonym of fracturing), but it is difficult to directly observe cracking on ice shelves. In this paper, we track cracks on Pine Island Glacier, an ice shelf in Antarctica that is particularly vulnerable to collapse. We see cracks in pictures taken by satellites. Cracking causes the ice shelf to shake up and down, which we record using the same equipment that records earthquakes. We record shaking located at a set of cracks at the side of the ice shelf and at the tip of a single massive crack called a rift. Rift cracking seems related to the speed that the ice shelf is flowing. We also use a computer simulation of shaking to learn about the details of the crack process. Our simulation suggests that the crack process might be more complicated than a single crack opening evenly at a constant rate.

2 Introduction

Ice shelf fracture is a fundamental process controlling the stability of marine ice sheets and associated sea level fluctuations (Seroussi et al., 2020). Fractures on ice shelves take on many forms including through-cutting rifts (Larour et al., 2004; Hulbe et al., 2010; Lipovsky, 2020), smaller-scale basal and surface crevasses (Rist et al., 2002; McGrath et al., 2012), hydraulic fracturing (Weertman, 1973; Banwell et al., 2013), and cliff failure (Clerc et al., 2019). Despite decades of progress, understanding of ice shelf fracture remains significantly hindered by a lack of direct observation (Benn et al., 2007). For this reason, previous studies have examined icequakes generated by rapid ice shelf fracture growth (Von der Osten-Woldenburg, 1990; Bassis et al., 2007, 2008; Heeszel et al., 2014; Hammer et al., 2015; Olinger et al., 2019; Chen et al., 2019; Winberry et al., 2020; Aster et al., 2021). Here, we use flexural gravity waves to quantify fracturing of the Pine Island Glacier (PIG) Ice Shelf.

PIG contributes more to present day global sea level rise than any other glacier (Shepherd et al., 2018). Ice mass loss on PIG is thought to be due to the retreat of the floating ice shelf (Joughin, Shapero, Smith, et al., 2021), the latter being caused by interactions between ocean forcing (Christianson et al., 2016; Joughin, Shapero, Dutrieux, & Smith, 2021) and fracturing processes (MacGregor et al., 2012). Upon creating a catalog of impulsive flexural gravity wave events on PIG, we examine the relationship between crevasse growth, large-scale rift propagation, shear margin processes, and ice shelf acceleration.

We focus on icequakes that travel as flexural gravity waves. Flexural gravity waves are unique to floating structures such as ice shelves; they have as their restoring force both elasticity and buoyancy and are therefore a type of hybrid seismic-water wave (Ewing & Crary, 1934). Many sources have been observed to generate flexural gravity waves on ice shelves including ocean swell (Williams & Robinson, 1981), tsunamis (Bromirski et al., 2017), and airplane landings (MacAyeal et al., 2009). This wave mode is strongly dispersive (Ewing & Crary, 1934), which can make waveform analysis difficult and necessitates careful modelling (Sergienko, 2017; Mattsson et al., 2018; Lipovsky, 2018). Despite this challenge, flexural gravity waves are useful tools to study ice shelf processes because because, while direct body waves in ice shelves are often not observed at distances greater than a few ice thickness (Zhan et al., 2014), flexural gravity waves are often observed to travel long distances from their exciting source (Williams & Robinson, 1981).

MacAyeal et al. (2009) appears to have been the first to propose that that fracturing processes in ice shelves may act as seismic sources that generate flexural gravity waves. MacAyeal et al. (2009) considered water motion in a deforming rift and motion of detaching blocks from the ice front as two such sources. Here, we hypothesize that crevasse growth generates flexural gravity waves. This creates a novel mechanical problem with regards to the representation of crevasse growth a seismic source. In an elastic body, motion that is discontinuous across a planar interface (i.e., a dislocation) such as a fault or a crevasse is equivalently represented by a moment tensor (Aki & Richards, 2002, Equation 3.20). While this description applies to elastic wave propagation in an ice shelf, it may not necessarily be the most useful way to approach the problem. For example, if no body waves are detectable, then the radiation pattern predicted by (Aki & Richards, 2002, Equation 3.20) will not be observed.

The simplest model that captures flexural gravity wave propagation is that of a buoyantly supported elastic beam (Sergienko, 2017; Mattsson et al., 2018). Because this model only has the vertical component motion as an independent variable, classical dislocations require an indirect parameterization in terms of either vertical motion or one of its derivatives: tilt, moment, vertical shear, and vertical point load (Hetenyi, 1946). In our analysis, we examine how these various types of excitation act during ice shelf crevasse growth. We begin our fracture analysis by describing a timeline of events with the use of satellite imagery.

3 Analysis of Satellite Imagery and Positioning

We track visible fracturing on PIG using images collected by the TerraSAR-X satellite (Pitz & Miller, 2010) from 2012 to 2014. At the start of our study period in January 2012 (dictated by the seismic/geodetic deployment, detailed below), the primary visible fractures are the rift, $\sim$20 large cracks extending into the ice shelf from northern shear margin, and $\sim$10 cracks extending into the ice shelf at the southern edge of the nascent iceberg (Figure 1a, left). By January 2013, the main rift had propagated a few kilometers without significant widening, and two wing cracks (Renshaw & Schulson, 2001) opened at the rift tip (Figure 1a, right). One of the cracks at the northern shear margin extended 7 km and connected to the rift between May 8 and May 11, 2012. The other northern shear margin cracks extended and widened, at least two new cracks initiated near Evans Knoll, and one of cracks at the southern edge of the nascent iceberg extended to within a kilometer of the rift tip.

During the first four months of 2013, the wing cracks near the rift tip extended and widened. In early July 2013, a block of ice calved along a wing crack at the southern edge of the nascent iceberg near the rift tip (Figure 1b). After this preliminary calving event, the only connection between the nascent iceberg and the ice shelf was a 2 km wide strip of ice between the ocean and a wing crack. Over the next few months, we observe significant widening of the rift, likely due to the iceberg beginning to drift away from the ice shelf. Iceberg B-31 calved in November 2013 (Figure 1c) when left lateral motion of the iceberg pried open a large wing crack near the rift tip until the strip of ice stabilizing the iceberg broke off, allowing Iceberg B-31 to drift into the sea. By the end of 2013, many fractures in the northern shear margin had extended and calved smaller icebergs, and several new fractures had initiated near Evans Knoll.

We furthermore examine Global Positioning System (GPS) speed timeseries derived from five continuous GPS stations. The GPS stations were co-located with seismometers (described below); the station locations are shown in Figure 2. Our GPS processing strategy is described in Supporting Text S1. Figure 3a plots the GPS-derived ice shelf velocity. We find that ice speed at PIG decreases from over 11 m/day in January 2012 to 10.8 m/day in April 2013. Then, ice speed drops to 10.6 m/day for around a month beginning May 2013. Following this rapid slowdown, ice speed begins to increase, reaching nearly 11 m/day by the end of 2013. The GPS ice speed we compute here is consistent with a previous study utilizing the same dataset (Christianson et al., 2016).

4 Analysis of Seismograms

We examine seismic and GPS data from five sites on PIG (Stanton et al., 2013). The instruments were deployed in January 2012 and retrieved in December 2013, providing about two years of continuous data. The seismic stations were deployed in a cross shape with 5 km aperture at the center of the ice shelf (Figure 2). Each site consisted of a three component Nanometrics Trillium 120 Broadband seismometer and a Quanterra Q330 digitizer (David Holland & Robert Bindschadler, 2012). Seismic data was sampled at 100 Hz, and we removed the instrumental response on the frequency band 0.001 Hz to 45 Hz. Each seismometer was co-located with a GPS station. We compare the seismic records with the timeline constructed using GPS time series and TerraSAR-X satellite imagery.

In the seismic dataset, we observe events with an abrupt onset and with high frequencies that arrive before low frequencies. This type of dispersion is characteristic of flexural gravity waves, which have previously been described on ice shelves (MacAyeal et al., 2009; Sergienko, 2017; Mattsson et al., 2018). The dispersion is the opposite of typical surface waves from tectonic earthquakes, where low frequencies arrive first because seismic wave speeds generally increase with depth. Following this interpretation, we design a workflow to identify and analyze flexural gravity waves generated by icequakes. For simplicity, in the rest of the text we refer to impulsive flexural gravity wave events as icequakes.

To detect icequakes in the dataset, we design a two-stage detection scheme that identifies broadband, dispersive seismic events. Our detection approach, described in Supporting Text S2, uses a dual-band short term average/long term average (STA/LTA) detector that is enhanced through template matching (Allen, 1978; Gibbons & Ringdal, 2006). This detection approach results in a preliminary catalog of 22,119 events. Inspection of the preliminary catalog reveals two main families of events: one with clear high-frequency-first dispersion and one which is dominantly monochomatic. In order to focus on the former, and consistent with our focus on icequake flexural gravity waves, we undertake waveform clustering using a modified K-Shape algorithm (Paparrizos & Gravano, 2016). Our modifications specifically enable the analysis of multi-component seismic data (see Text S2). Visual analysis of the clustered catalog demonstrates the efficacy of our approach in isolating flexural gravity waves (Fig. 3). Our final catalog contains 8,184 likely icequakes.

We next determine icequake locations for all events in our final catalog. Given the poor distribution of the stations with respect to fracture locations, we employ single-station approaches to locating icequakes. We compute epicentral back-azimuths by analyzing the polarization direction of recorded horizontal waves. We apply principle component

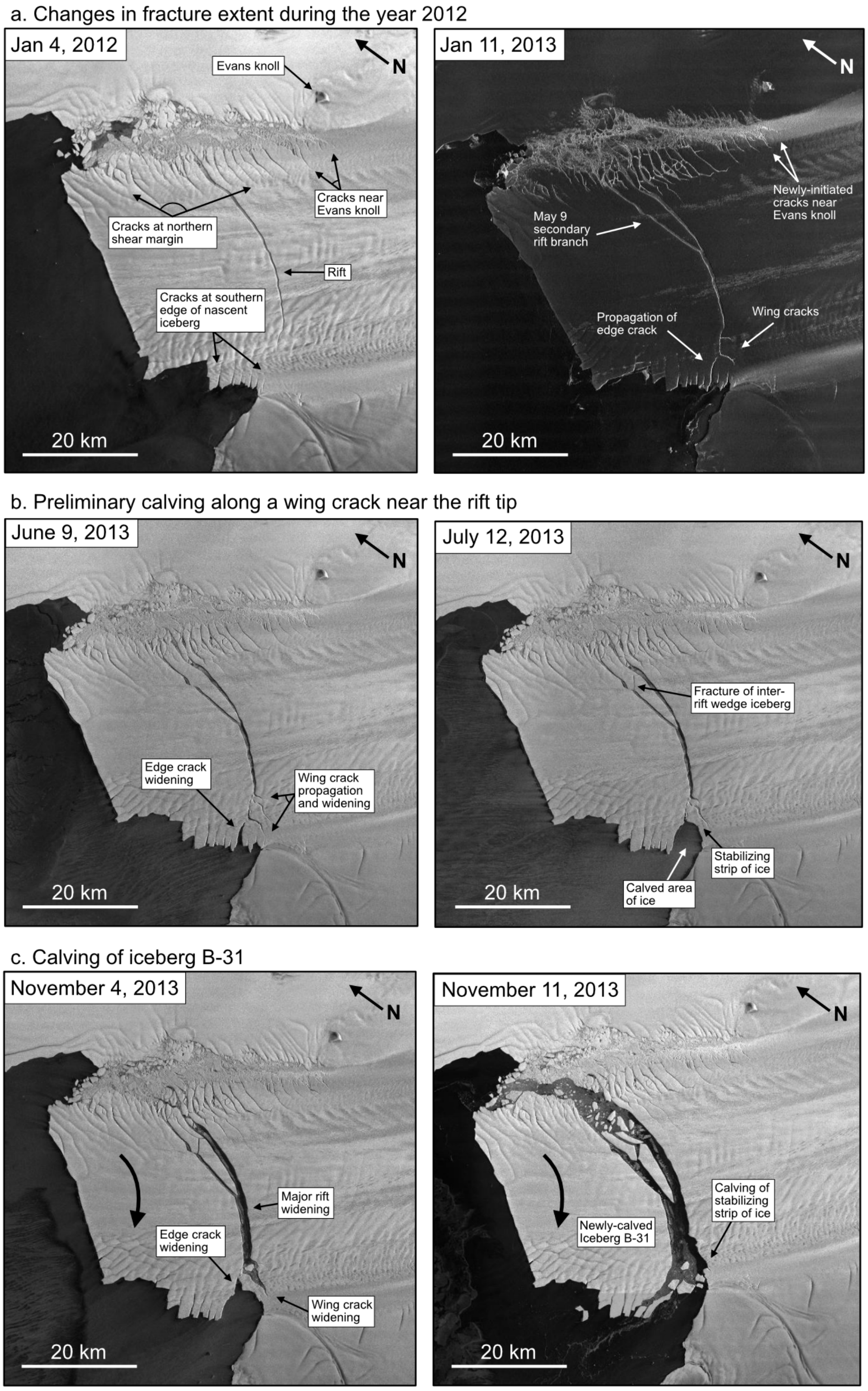

Figure 1. TerraSAR-X images showing an overview of fracture development at PIG from 2012 to 2014. Large arrow in panels c. and d. show sense of motion of the iceberg. See text for full discussion.

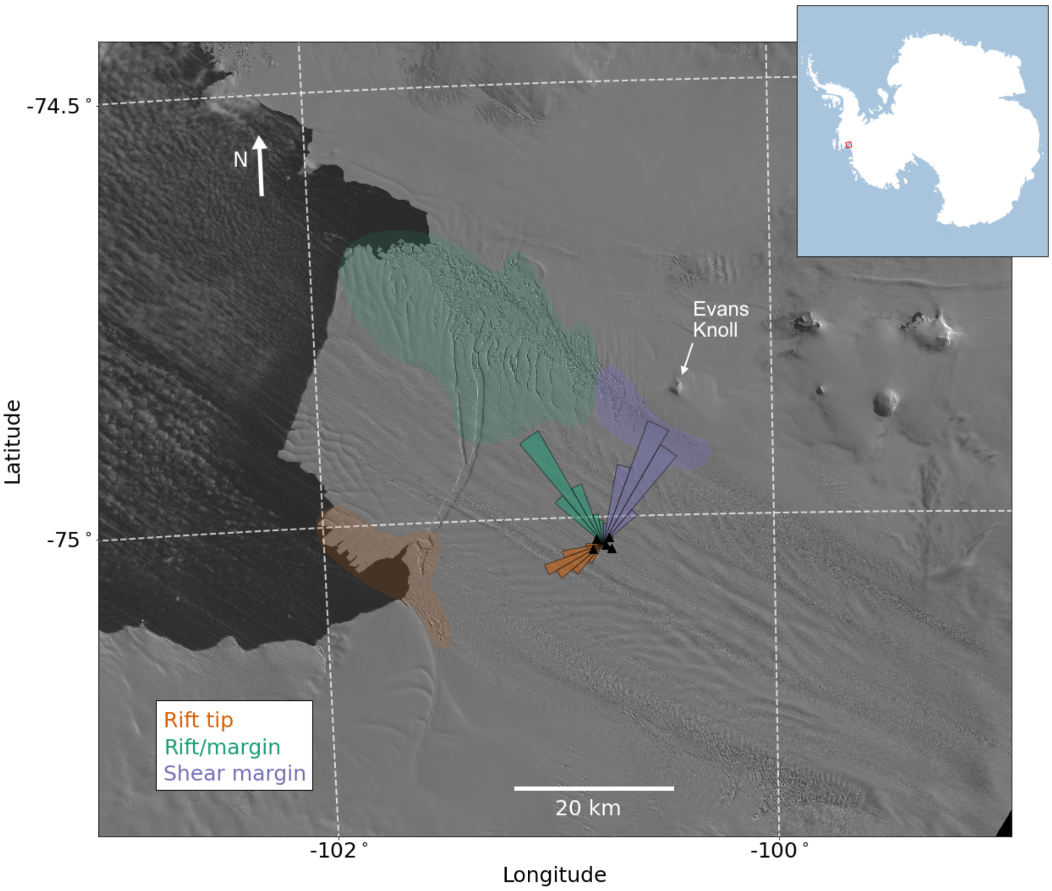

Figure 2. Locations of fracture events detected using template matching. Rift-tip event back-azimuths are plotted as orange rays. Rift/margin-event back-azimuths are plotted as purple rays. Shear-margin event back-azimuths are plotted as green rays. Likely source regions for each group are shown by colored polygons. PIG array seismic stations are plotted as black triangles. Background LANDSAT imagery is from October 2013 (courtesy of the United States Geological Survey).

analysis (PCA) to the horizontal component seismograms to retrieve polarization directions. The polarization provides a 180 degree ambiguity, so we find the direction of propagation based on which station recorded the first arrival using a robust algorithm (see Text S3).

We locate all of the 8,184 icequakes to one of three distinct source regions: the rift tip, the body of the rift and nearby shear margin ("rift/margin"), and the northeast shear margin near Evan's knoll ("shear margin"), which are depicted in Figure 2. These spatial groups correspond to 22%, 29%, and 40% of the catalog, respectively, with 9% of events having indeterminate locations. Figure 2 shows the azimuthal histograms of the three clusters. In the following, all of the waveforms that we analyze are filtered to the frequency range between 100 s and 1 s.

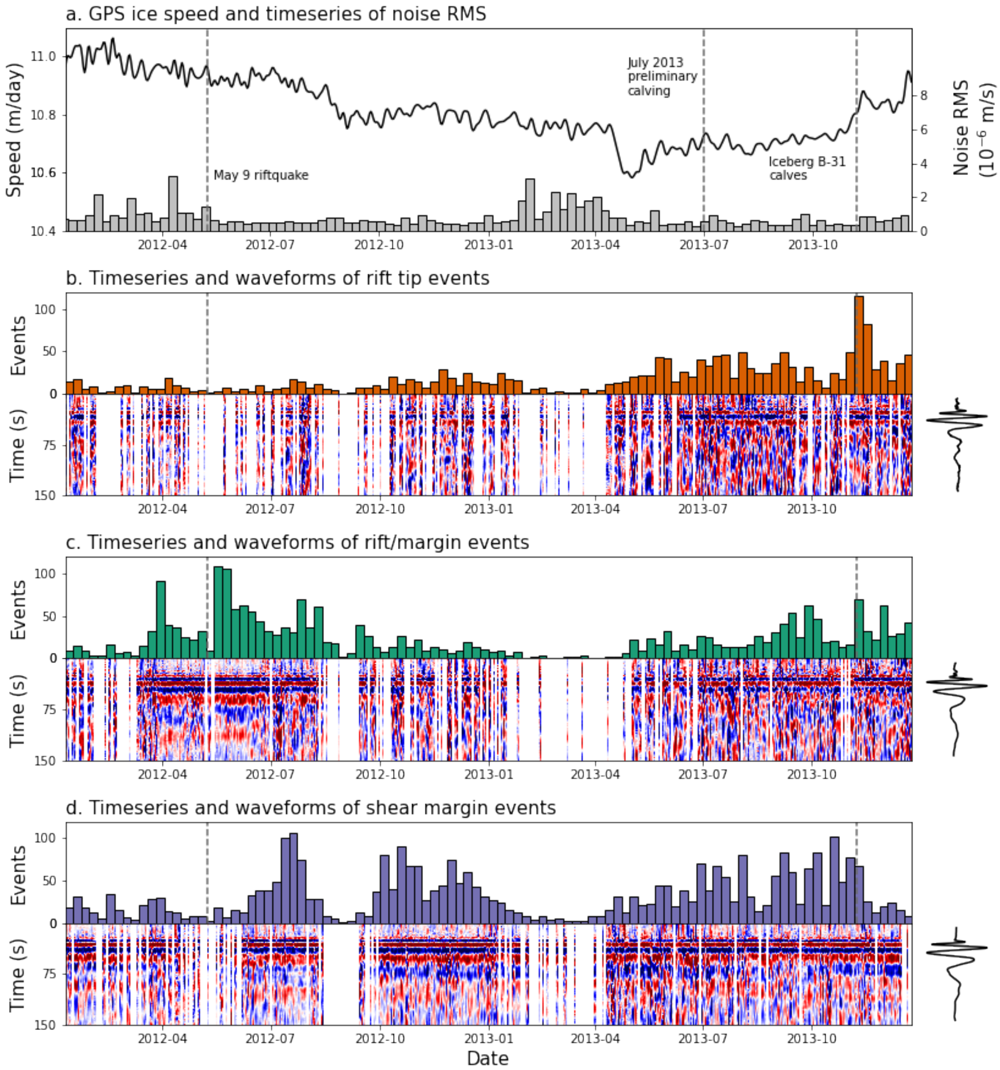

Figure 3. Timing and waveforms of icequakes detected using template matching. (a) GPS-derived ice velocity (black line) and average noise calculated with Root Mean Square amplitudes (gray bars). Noise is highest in the Antarctic summer, when minimal sea ice is present to attenuate ocean-generated noise, reducing detectability in January, February, and March. (b) Rift-tip events. Weekly timeseries of rift tip event times is shown by orange bars. Daily vertical (HHZ) waveform stacks of detected rift tip events are plotted beneath. Overall rift-tip event stack is shown to the right. (c) Same as (b) for northwest shear-margin events, color-coded in green. (d) Same as (b) for northeast shear-margin events color-coded in purple.

5 Relationships Between Icequakes and Ice Shelf Behavior

5.1 Rift tip

The rift-tip icequakes are coincident in space and time with several fracturing processes including rift propagation, wing cracking, small scale calving within the rift, smaller-scale crevassing, and calving along the southern edge of the nascent iceberg. Rift tip events occurred more frequently in 2013 than in 2012 (Figure 3b). No week of 2012 contained more than 30 events, while 17 weeks of 2013 contained more than 30 icequakes (9.4 versus 17.5 icequakes/week). Weekly icequake counts increased past the peak level seen in 2012 on May 21, 2013 and remain elevated until the end of the deployment. This period of elevated rift tip seismicity corresponds to the phase of significant wing crack growth and rift widening observed in imagery.

Peak levels of rift-tip seismicity were observed during the calving of Iceberg B-31 in the week of November 5, 2013. That week had 115 rift-tip events, the highest event count of any week across all three source regions. Furthermore, elevated rift-tip icequake activity in 2013 corresponds to a period of accelerated ice velocities (Figure 3a). Christianson et al. (2016) hypothesize that the overall pattern of ice velocities tracks a time-lagged response to ocean melting. Walker and Gardner (2019) propose that such melting near and within rifts promotes fracture. The observed connection in time between rift tip fracture and accelerated ice velocities demonstrates that rift growth and PIG is sensitive to localized thinning, changes in ice dynamics, or a combination of both. At the present time, however, we are unable to confirm whether local or more distant melt-related feedbacks are responsible for the observed fracturing.

5.2 Rift/margin

The rift/margin icequakes are coincident in space and time with the growth of ∼20 rifts formed in the northwest shear zone, as well as smaller-scale fractures and widening of the main rift itself. Rift/margin icequakes occurred more frequently in 2012 than in 2013. 18 weeks of 2012 contained greater than 30 icequakes, while only 10 weeks of 2013 contained greater than 30 icequakes (27.7 versus 23.5 icequakes/week). The timing of icequakes in the rift/margin group is independent of ice speed. Peak levels of rift/margin seismicity were observed during the week of May 15, 2012, which contained 109 rift/margin icequakes. Rift/margin icequakes reach peak seismicity rates in the weeks following the opening of the secondary rift branch in May 2012, suggesting that the crack opening caused aftershock-like seismicity and/or destabilized the margin, enhancing the growth of nearby fractures.

5.3 Shear margin

The shear-margin icequakes are coincident in space and time with the initiation of new cracks and growth of extant cracks near Evans Knoll. This area marks the transition from a primarily intact shear margin upstream of Evans Knoll to a highly fractured shear margin downstream of Evans Knoll. Imagery shows that multiple fractures longer than 1 km were initiated in this area during 2012 and 2013 (Figure 1). Shear-margin icequakes occurred at an approximately equal rate in 2012 and 2013. 20 weeks of 2012 and 2013 contained greater than 30 icequakes (29.6 versus 30.3 icequakes/week). Peak levels of shear margin seismicity were observed during the week of October 15, 2013, which contained 99 shear-margin icequakes. Shear-margin icequakes do not exhibit any prominent temporal trends and appear independent of ice velocity. The shear margin experiences the highest overall level of seismic activity, suggesting that the transition point from intact to fractured ice near Evans Knoll experiences higher stress concentrations than either the rift tip or the rift/margin regions, consistent with rift modeling (Lipovsky, 2020).

6 Icequake Source Analysis

We next estimate the distribution of forces that gives rise to the observed seismograms. We do this by removing wave propagation effects from the observed seismograms using a theoretical and numerically computed Green's function. Our catalog was designed to represent icequakes that mostly consist of flexural gravity waves. We therefore model the vertical seismograms using the simplest model that gives rise to flexural gravity waves, the dynamic floating beam equation (Ewing & Crary, 1934; Squire & Allan, 1977),

$$\rho_i h_i \frac{\partial^2 w}{\partial t^2} + D\frac{\partial^4 w}{\partial x^4} + \rho_w g w + \rho_w \frac{\partial \phi}{\partial t} = P, \tag{1}$$

where $D \equiv EI = Eh_i^3/[12(1-\nu^2)]$ is the flexural rigidity with second moment of area $I = \int_{-h_i/2}^{h_i/2} z^2 dz$, E is the Young's modulus of ice, ν is the Poisson's ratio of ice, t is time, x is horizontal position, g is gravitational acceleration constant, h_i is the ice thickness, ρ_i is the density of ice, ρ_w is the density of water, w is the vertical displacement of the beam, ϕ is the ocean surface velocity potential, and P is an applied point load. From left to right, the terms in Equation (1) represent inertia, flexure of the ice shelf, buoyancy, and ocean surface waves generated at the ice-water interface. In the following, we use locally-averaged ice thickness $h_i = 400$ m (Shean et al., 2019), the water depth $h_w =$ 590 m (Fretwell et al., 2013).

We obtain the Green's function of the floating beam equation as the impulse response of the mechanical system to a point load (force per unit length) source. Rewriting Equation 1 using the linear operator $\mathcal{A}$ as $\mathcal{A}w = P$, the Green's function equation can then be written as $\mathcal{A}G = \delta(x)\delta(t)$. In Supporting Text S3, we derive a frequency-wavenumber solution for G that we are able to analytical invert in the time domain and numerically invert in the frequency domain. In Text S3 we also derive the Green's function G_m that is the vertical displacement response to a point moment source.

We follow two lines of inquiry to relate the calculated Green's functions to our icequake catalog. First, we deconvolve Green's functions from waveform stacks of our three spatial groups (Section 5) in order to estimate the source load or moment distribution. Second, we carry out sensitivity tests on our results in order to understand: 1. our ability to resolve static changes in load or moment and 2. to understand the influence of ice thickness and of our assumption of uniform ice thickness.

Figure 4 illustrates that a given vertical displacement seismogram (far right) may equivalently be represented as a point moment (Figure 4a and b) or an point load (Figure 4c and d). This figure shows our deconvolution result for the rift tip group of icequakes. The equivalent analysis for the other two groups of events is given in the Supporting Figures. We discuss the differences between point moment and point load sources in Section 6.

We examine the sensitivity of our deconvolution to the assumed value for the ice thickness by varying the ice thickness between 300 and 500 m (Supporting Figures S3-5). For the rift-tip group, we find source durations ranging from 30.48 to 50.00 s and amplitudes ranging from 2.69 to 6.90 MPa·m (point moment) and 3.83 to 8.62 kPa (point load). For the rift/margin group, we find source durations ranging from 19.52 to 48.57 s and amplitudes ranging from 3.82 to 12.55 MPa·m (point moment) and from 5.05 to 14.02 kPa (point load). Finally, for the shear-margin group, we find source durations ranging from 27.14 to 36.67 s and amplitudes ranging from 5.60 to 14.89 MPa·m (point moment) and from 8.04 to 12.97 kPa (point load).

Our resulting source time series for moment and point load generally exhibit one or several pulses of activity followed by a return to zero (Figure 4). Source time functions derived from body waves in an elastic medium result in estimates of moment rate (Aki & Richards, 2002, Equation 4.32,). Here, however, our deconvolution is sensitive

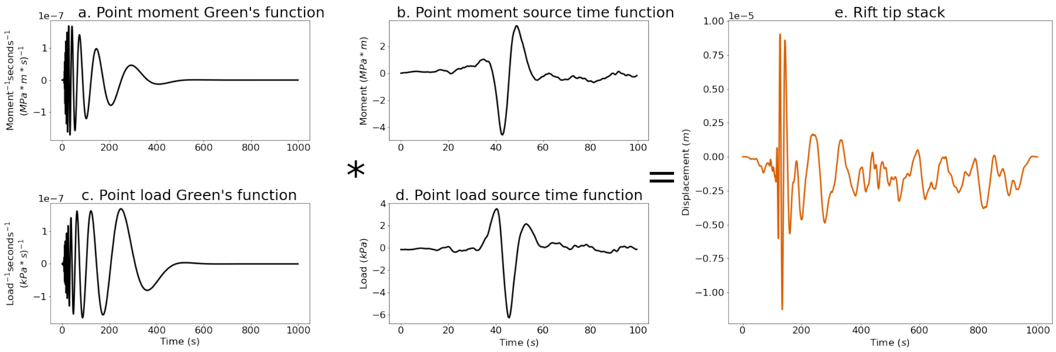

Figure 4. Green's functions and source time functions for rift tip events. (a) Theoretical Green's function for a point moment source located at a distance of 25 km, which is approximately the distance from PIG seismic array to the rift tip. (b) Source time function retrieved by deconvolving the point moment Green's function from the stack of rift tip vertical displacement waveforms. (c) Theoretical Green's function for a point load source located at a distance of 25 km. (d) Source time function retrieved by deconvolving the point load Green's function from the stack of rift tip vertical displacement waveforms. (e) Stack of rift tip vertical displacement waveforms obtained by aligning waveforms to a master event and taking the mean waveform on the frequency band 0.01-1 Hz.

not to the rate of change of point load or moment, but instead to a point load and moment. This complicates the interpretation of the estimated source time series because it suggests that the icequakes represent the application and subsequent removal of some point load or moment. This physically counterintuitive situation motivates an examination of the sensitivity of our deconvolution to static offsets. We therefore calculate synthetic seismograms forced by a step in moment or point load (Supporting Figures S6-S8). We find that in some cases the step function provides an acceptable fit to the observations, which is probably due to limitations of the Fourier transform of non-periodic functions. We therefore conclude that our model is not clearly able to resolve differences in the source time series at low frequencies.

7 Discussion of icequake source physics

We have cataloged icequakes that propagate as flexural gravity waves. We then deconvolved wave propagation effects from icequake waveform stacks in order to estimate the distribution of forces that act at the icequake source. This workflow lead us to make several assumptions about the nature of the icequake source that we now discuss.

We examined the situation where the icequake source was either an applied point bending moment or point load. Both cases can be justified with physical reasoning. First, when a basal crevasse opens and fills with water, the downward-acting ice overburden stress at the top of the crevasse is greater in magnitude than the upward-acting buoyancy stress exerted by water filling the crevasse. This applies a downward point load to the ice shelf. Second, when a crevasse opens and fills with water, the horizontal ice overburden stress along the walls of the crevasse is greater in magnitude than the horizontal buoyancy stress exerted by the water filling the crevasse. In addition, the difference in magnitude between these two stresses decreases with depth such that the walls of a crevasse are subject to stress gradient. This applies a bending moment to the ice shelf. These two mechanisms may also act in concert and simultaneously apply a moment and point load to the ice shelf. We choose not to pursue this such hybrid sources at the present time, however, because the simplicity of our model –specifically the assumptions of uniform ice thickness and two-dimensional geometry– suggests that additional source complexity is not warranted prior to improvements in these other areas.

The timescale of the source process, however, is constrained independent of the exact force distribution assumed in the deconvolution. Our source analysis implies that the recorded flexural gravity waves were generated by fracturing process with approximately 20-50 s duration. At this timescale, the observed waves must have been generated by brittle fracture, not by viscous deformation. This 20-50 s timescale is extremely slow compared, for example, to tectonic earthquakes, where earthquake duration scales like $10^{M/2}$ with earthquake moment M and 20 s duration is associated with a $M = 7$ earthquake (Ekström et al., 2003).

What process sets the duration of the observed icequakes? The above scaling for tectonic earthquakes is based on the reasoning that the duration is set by the time required for a shear crack to propagate across a fault of length L and by assuming a shear cracks that tends towards propagation at inertial velocities (either the shear or dilatational wave speed v_s or v_p) (Freund, 1998). In our system, however, we expect that water plays a limiting role in the speed of fracture propagation that may not be present in tectonic earthquakes. The propagation of fluid filled basal crevasses is expected to occur at the crack wave speed (Lipovsky & Dunham, 2015). The crack wave speed is much slower than the inertial velocities and could plausibly be in the range of 1-100 m/s for basal crevasses in ice shelves. These velocities would suggest source length scales on the order of meters to hundreds of meters. A second plausible explanation is that long durations may be explained by the coalescence of many smaller individual fractures that open successively. And yet another explanation is that there could be significant horizontal propagation which is not captured in our model. We expect that more detailed near-source observations would be able to distinguish between these possible scenarios.

Regardless of the cause of slow ruptures, we estimate point load source amplitudes on the order of 1-10 kPa. Assuming crack opening occurs below the waterline, a point load of 10 kPa would result from displacing about 11 m of ice with water during vertical crevasse growth.

8 Conclusions

We detect and locate icequakes that propagate as flexural gravity waves on the Pine Island Glacier ice shelf from 2012 to 2014. When compared to satellite imagery, the back-azimuthal distribution of the detected events suggests that the icequakes were generated by fractures at the tip of a large rift and in two distinct portions of the northern shear margin. Most of the events were generated at the shear margin near Evans Knoll, in agreement with imagery that suggests significant fracture initiation. Increased fracturing at the rift tip is associated with increased ice speed in 2013, interpreted as due to elevated basal melting (Christianson et al., 2016). We attribute this relationship to melt-driven thinning that elevated rift tip stress concentrations. We use a simple model of flexural gravity waves to constrain the source of the recorded waves. We find that the observed waves have a source duration between 20-50 s. This timescale implies that a brittle fracture process generated the waves. Our analysis therefore confirms the role of brittle processes in the long-term evolution of marine ice sheets.

Acknowledgments

SDO and BPL were supported by the National Science Foundation (NSF) Office of Polar Programs (OPP) award #1853896. SDO was also supported by the startup funds of MAD at Harvard University in the Department of Earth and Planetary Sciences. The facilities of IRIS Data Services, and specifically the IRIS Data Management Center, were used for access to waveforms, related metadata, and/or derived products used in this study. IRIS Data Services are funded through the Seismological Facilities for the Advancement of Geoscience (SAGE) Award of the National Science Foundation under Cooperative Support Agreement EAR-1851048. The seismic and geodetic datasets were collected by David Holland and Robert Bindschadler (2012), and the seismic DOI is `https://doi.org/10.7914/sn/xc_2012`. The seismic instruments were provided by the Incorporated Research Institutions for Seismology (IRIS) through the PASSCAL Instrument Center at New Mexico Tech. Data collected is available through the IRIS Data Management Center. The facilities of the IRIS Consortium are supported by the National Science Foundation's Seismological Facilities for the Advancement of Geoscience (SAGE) Award under Cooperative Support Agreement EAR-1851048. Geodetic data are based on services provided by the GAGE Facility, operated by UNAVCO, Inc., with support from the National Science Foundation and the National Aeronautics and Space Administration under NSF Cooperative Agreement EAR-1724794. GPS processing was done using the GipsyX software, licensed to BWC at University of Washington. TerraSAR-X images were obtained using the freely-available EOWEB GeoPortal courtesy of the German Aerospace Center (DLR). Code to reproduce the processing workflow for this paper is currently hosted at `https://github.com/setholinger/rift_detection_location` and `https://github.com/setholinger/floatingBeamGF` for peer review and will be hosted on Zenodo shortly.

References

Aki, K., & Richards, P. G. (2002). *Quantitative seismology.*

Allen, R. V. (1978, 10). Automatic earthquake recognition and timing from single traces. *Bulletin of the Seismological Society of America*, *68*(5), 1521-1532. Retrieved from `https://doi.org/10.1785/BSSA0680051521` doi: 10.1785/BSSA0680051521

Aster, R. C., Lipovsky, B. P., Cole, H. M., Bromirski, P. D., Gerstoft, P., Nyblade, A., ... Stephen, R. (2021). Swell-triggered seismicity at the near-front damage zone of the ross ice shelf. *Seismological Research Letters*.

Banwell, A. F., MacAyeal, D. R., & Sergienko, O. V. (2013). Breakup of the larsen b ice shelf triggered by chain reaction drainage of supraglacial lakes. *Geophysical Research Letters*, *40*(22), 5872–5876.

Bassis, J. N., Fricker, H. A., Coleman, R., Bock, Y., Behrens, J., Darnell, D., ... Minster, J.-B. (2007). Seismicity and deformation associated with ice-shelf rift propagation. *Journal of Glaciology*, *53*(183), 523–536. doi: 10.3189/002214307784409207

Bassis, J. N., Fricker, H. A., Coleman, R., & Minster, J.-B. (2008). An investigation into the forces that drive ice-shelf rift propagation on the amery ice shelf, east antarctica. *Journal of Glaciology*, *54*(184), 17–27. doi: 10.3189/002214308784409116

Benn, D. I., Warren, C. R., & Mottram, R. H. (2007). Calving processes and the dynamics of calving glaciers. *Earth-Science Reviews*, *82*(3-4), 143–179.

Bromirski, P. D., Chen, Z., Stephen, R. A., Gerstoft, P., Arcas, D., Diez, A., ... Nyblade, A. (2017). Tsunami and infragravity waves impacting antarctic ice shelves. *Journal of Geophysical Research: Oceans*, *122*(7), 5786-5801. Retrieved from `https://agupubs.onlinelibrary.wiley.com/doi/abs/10.1002/2017JC012913` doi: https://doi.org/10.1002/2017JC012913

Chen, Z., Bromirski, P., Gerstoft, P., Stephen, R., Lee, W. S., Yun, S., ... Nyblade, A. (2019). Ross ice shelf icequakes associated with ocean gravity wave activity. *Geophysical Research Letters*, *46*(15), 8893–8902.

Christianson, K., Bushuk, M., Dutrieux, P., Parizek, B. R., Joughin, I. R., Alley, R. B., ... Holland, D. M. (2016). Sensitivity of pine island glacier to observed ocean forcing. *Geophysical Research Letters*, *43*(20), 10,817-10,825. Retrieved from `https://agupubs.onlinelibrary.wiley.com/doi/abs/`

10.1002/2016GL070500 doi: 10.1002/2016GL070500

Clerc, F., Minchew, B. M., & Behn, M. D. (2019). Marine ice cliff instability mitigated by slow removal of ice shelves. *Geophysical Research Letters*, *46*(21), 12108–12116.

David Holland, & Robert Bindschadler. (2012). *Observing pine island glacier (pig) ice shelf deformation and fracture using a gps and seismic network.* International Federation of Digital Seismograph Networks. Retrieved from https://www.fdsn.org/networks/detail/XC_2012/ doi: 10.7914/SN/XC_2012

Ekström, G., Nettles, M., & Abers, G. A. (2003). Glacial earthquakes. *Science*, *302*(5645), 622–624.

Ewing, M., & Crary, A. (1934). Propagation of elastic waves in ice. part ii. *Physics*, *5*(7), 181–184.

Fretwell, P., Pritchard, H. D., Vaughan, D. G., Bamber, J. L., Barrand, N. E., Bell, R., ... Zirizzotti, A. (2013). Bedmap2: improved ice bed, surface and thickness datasets for antarctica. *The Cryosphere*, *7*(1), 375–393. Retrieved from https://tc.copernicus.org/articles/7/375/2013/ doi: 10.5194/tc-7-375-2013

Freund, L. B. (1998). *Dynamic fracture mechanics.* Cambridge university press.

Gibbons, S. J., & Ringdal, F. (2006, 04). The detection of low magnitude seismic events using array-based waveform correlation. *Geophysical Journal International*, *165*(1), 149-166. Retrieved from https://doi.org/10.1111/j.1365-246X.2006.02865.x doi: 10.1111/j.1365-246X.2006.02865.x

Hammer, C., Ohrnberger, M., & Schlindwein, V. (2015). Pattern of cryospheric seismic events observed at ekström ice shelf, antarctica. *Geophysical Research Letters*, *42*(10), 3936–3943.

Heeszel, D. S., Fricker, H. A., Bassis, J. N., O'Neel, S., & Walter, F. (2014). Seismicity within a propagating ice shelf rift: The relationship between icequake locations and ice shelf structure. *Journal of Geophysical Research: Earth Surface*, *119*(4), 731-744. Retrieved from https://agupubs.onlinelibrary.wiley.com/doi/abs/10.1002/2013JF002849 doi: 10.1002/2013JF002849

Hetenyi, M. (1946). *Beams on elastic foundation.* Ann Arbor: University of Michigan Press.

Hulbe, C. L., LeDoux, C., & Cruikshank, K. (2010). Propagation of long fractures in the ronne ice shelf, antarctica, investigated using a numerical model of fracture propagation. *Journal of Glaciology*, *56*(197), 459–472. doi: 10.3189/002214310792447743

Joughin, I., Shapero, D., Dutrieux, P., & Smith, B. (2021). Ocean-induced melt volume directly paces ice loss from pine island glacier. *Science advances*, *7*(43), eabi5738.

Joughin, I., Shapero, D., Smith, B., Dutrieux, P., & Barham, M. (2021). Ice-shelf retreat drives recent pine island glacier speedup. *Science Advances*, *7*(24), eabg3080.

Larour, E., Rignot, E., & Aubry, D. (2004). Modelling of rift propagation on ronne ice shelf, antarctica, and sensitivity to climate change. *Geophysical research letters*, *31*(16).

Lipovsky, B. P. (2018). Ice shelf rift propagation and the mechanics of wave-induced fracture. *Journal of Geophysical Research: Oceans*, *123*(6), 4014-4033. doi: https://doi.org/10.1029/2017JC013664

Lipovsky, B. P. (2020). Ice shelf rift propagation: stability, three-dimensional effects, and the role of marginal weakening. *The Cryosphere*, *14*(5), 1673–1683. doi: 10.5194/tc-14-1673-2020

Lipovsky, B. P., & Dunham, E. M. (2015). Vibrational modes of hydraulic fractures: Inference of fracture geometry from resonant frequencies and attenuation. *Journal of Geophysical Research: Solid Earth*, *120*(2), 1080–1107.

MacAyeal, D. R., Okal, E. A., Aster, R. C., & Bassis, J. N. (2009). Seismic observations of glaciogenic ocean waves (micro-tsunamis) on icebergs and ice shelves. *Journal of Glaciology*, *55*(190), 193–206.

MacGregor, J. A., Catania, G. A., Markowski, M. S., & Andrews, A. G. (2012). Widespread rifting and retreat of ice-shelf margins in the eastern amundsen sea embayment between 1972 and 2011. *Journal of Glaciology*, *58*(209), 458–466.

Mattsson, K., Dunham, E. M., & Werpers, J. (2018). Simulation of acoustic and flexural-gravity waves in ice-covered oceans. *Journal of Computational Physics*, *373*, 230–252.

McGrath, D., Steffen, K., Scambos, T., Rajaram, H., Casassa, G., & Lagos, J. L. R. (2012). Basal crevasses and associated surface crevassing on the larsen c ice shelf, antarctica, and their role in ice-shelf instability. *Annals of glaciology*, *53*(60), 10–18.

Olinger, S. D., Lipovsky, B. P., Wiens, D. A., Aster, R. C., Bromirski, P. D., Chen, Z., ... Stephen, R. A. (2019). Tidal and thermal stresses drive seismicity along a major ross ice shelf rift. *Geophysical Research Letters*, *46*(12), 6644-6652. Retrieved from https://agupubs.onlinelibrary.wiley.com/doi/abs/10.1029/2019GL082842 doi: 10.1029/2019GL082842

Paparrizos, J., & Gravano, L. (2016, June). K-shape: Efficient and accurate clustering of time series. *SIGMOD Rec.*, *45*(1), 69–76. Retrieved from https://doi.org/10.1145/2949741.2949758 doi: 10.1145/2949741.2949758

Pitz, W., & Miller, D. (2010). The terrasar-x satellite. *IEEE Transactions on Geoscience and Remote Sensing*, *48*(2), 615-622. doi: 10.1109/TGRS.2009.2037432

Renshaw, C. E., & Schulson, E. M. (2001). Universal behaviour in compressive failure of brittle materials. *Nature*, *412*(6850), 897–900.

Rist, M., Sammonds, P., Oerter, H., & Doake, C. (2002). Fracture of antarctic shelf ice. *Journal of Geophysical Research: Solid Earth*, *107*(B1), ECV–2.

Sergienko, O. (2017, 07). Behavior of flexural gravity waves on ice shelves: Application to the ross ice shelf. *Journal of Geophysical Research: Oceans*, *122*. doi: 10.1002/2017JC012947

Seroussi, H., Nowicki, S., Payne, A. J., Goelzer, H., Lipscomb, W. H., Abe-Ouchi, A., ... others (2020). Ismip6 antarctica: a multi-model ensemble of the antarctic ice sheet evolution over the 21st century. *The Cryosphere*, *14*(9), 3033–3070.

Shean, D. E., Joughin, I. R., Dutrieux, P., Smith, B. E., & Berthier, E. (2019). Ice shelf basal melt rates from a high-resolution digital elevation model (dem) record for pine island glacier, antarctica. *The Cryosphere*, *13*(10), 2633–2656. Retrieved from https://tc.copernicus.org/articles/13/2633/2019/ doi: 10.5194/tc-13-2633-2019

Shepherd, A., Ivins, E., Rignot, E., Smith, B., Van Den Broeke, M., Velicogna, I., ... others (2018). Mass balance of the antarctic ice sheet from 1992 to 2017. *Nature*, *558*, 219–222.

Squire, V. A., & Allan, A. (1977). *Propagation of flexural gravity waves in sea ice.* Centre for Cold Ocean Resources Engineering, Memorial University of Newfoundland.

Stanton, T. P., Shaw, W., Truffer, M., Corr, H., Peters, L., Riverman, K., ... Anandakrishnan, S. (2013). Channelized ice melting in the ocean boundary layer beneath pine island glacier, antarctica. *Science*, *341*(6151), 1236–1239.

Von der Osten-Woldenburg, H. (1990). Icequakes on ekström ice shelf near atka bay, antarctica. *Journal of Glaciology*, *36*(122), 31–36.

Walker, C., & Gardner, A. (2019). Evolution of ice shelf rifts: Implications for formation mechanics and morphological controls. *Earth and Planetary Science Letters*, *526*, 115764. Retrieved from https://www.sciencedirect.com/science/article/pii/S0012821X1930456X doi: https://doi.org/10.1016/

j.epsl.2019.115764
Weertman, J. (1973). Can a water-filled crevasse reach the bottom surface of a glacier. *IASH publ*, *95*, 139–145.
Williams, R., & Robinson, E. (1981). Flexural waves in the ross ice shelf. *Journal of Geophysical Research: Oceans*, *86*(C7), 6643–6648.
Winberry, J. P., Huerta, A. D., Anandakrishnan, S., Aster, R. C., Nyblade, A. A., & Wiens, D. A. (2020). Glacial earthquakes and precursory seismicity associated with thwaites glacier calving. *Geophysical Research Letters*, *47*(3), e2019GL086178. Retrieved from `https://agupubs.onlinelibrary.wiley.com/doi/abs/10.1029/2019GL086178` (e2019GL086178 2019GL086178) doi: 10.1029/2019GL086178
Zhan, Z., Tsai, V. C., Jackson, J. M., & Helmberger, D. (2014). Ambient noise correlation on the amery ice shelf, east antarctica. *Geophysical Journal International*, *196*(3), 1796–1802.

Figure 1.

a. Changes in fracture extent during the year 2012
Jan 4, 2012
N
Evans knoll
Cracks near Evans knoll
Cracks at northern shear margin
Rift
Cracks at southern edge of nascent iceberg
20 km
Jan 11, 2013
N
Newly-initiated cracks near Evans knoll
May 9 secondary rift branch
Propagation of edge crack
Wing cracks
20 km
b. Preliminary calving along a wing crack near the rift tip
June 9, 2013
N
Edge crack widening
Wing crack propagation and widening
20 km
July 12, 2013
N
Fracture of inter-rift wedge iceberg
Stabilizing strip of ice
Calved area of ice
20 km
c. Calving of iceberg B-31
November 4, 2013
N
Major rift widening
Edge crack widening
Wing crack widening
20 km
November 11, 2013
N
Calving of stabilizing strip of ice
Newly-calved Iceberg B-31
20 km

Figure 2.

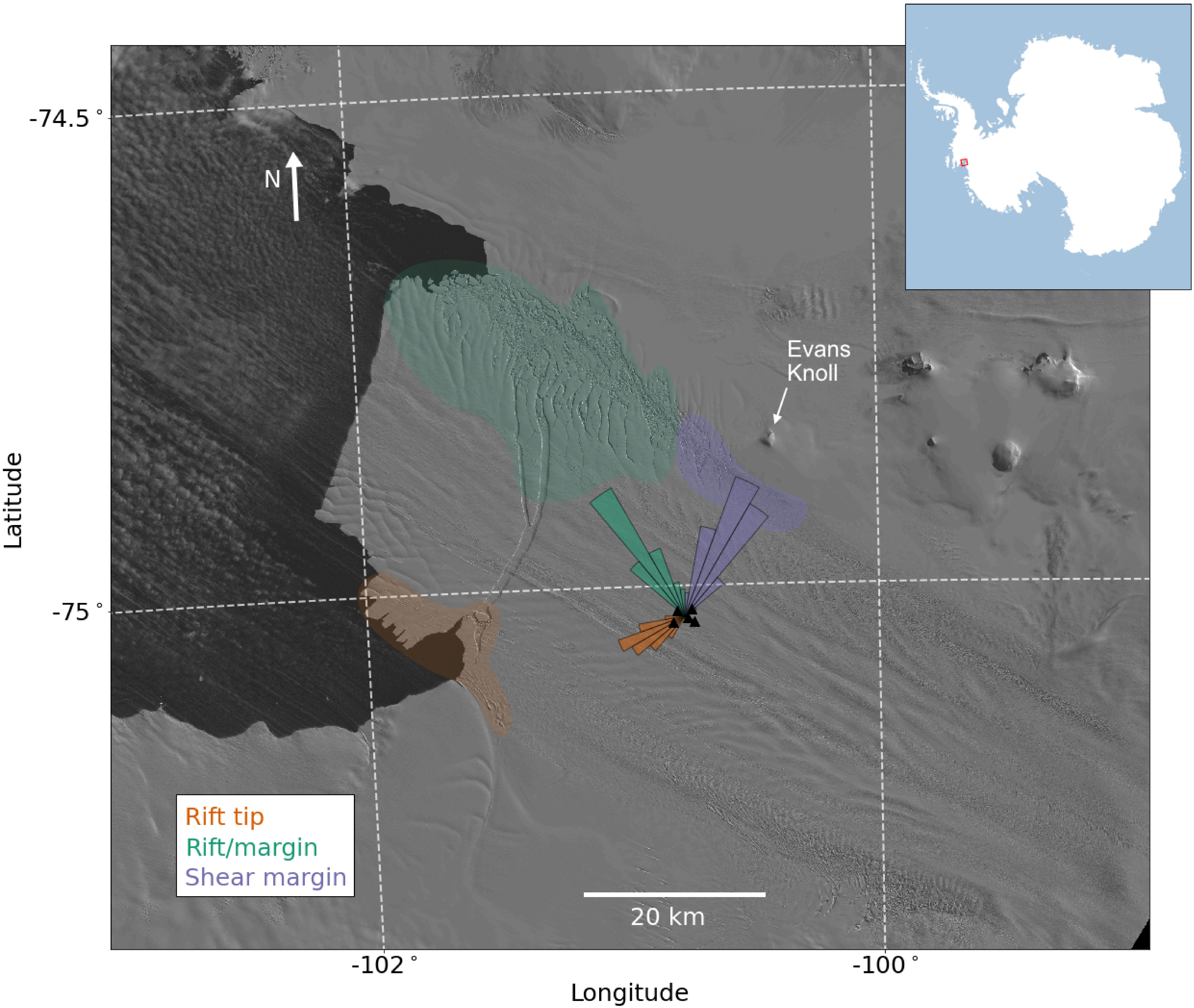
-74.5 °
-75 °
Latitude
-102 °
-100 °
Longitude
N
Evans Knoll
20 km
Rift tip
Rift/margin
Shear margin

Figure 3.

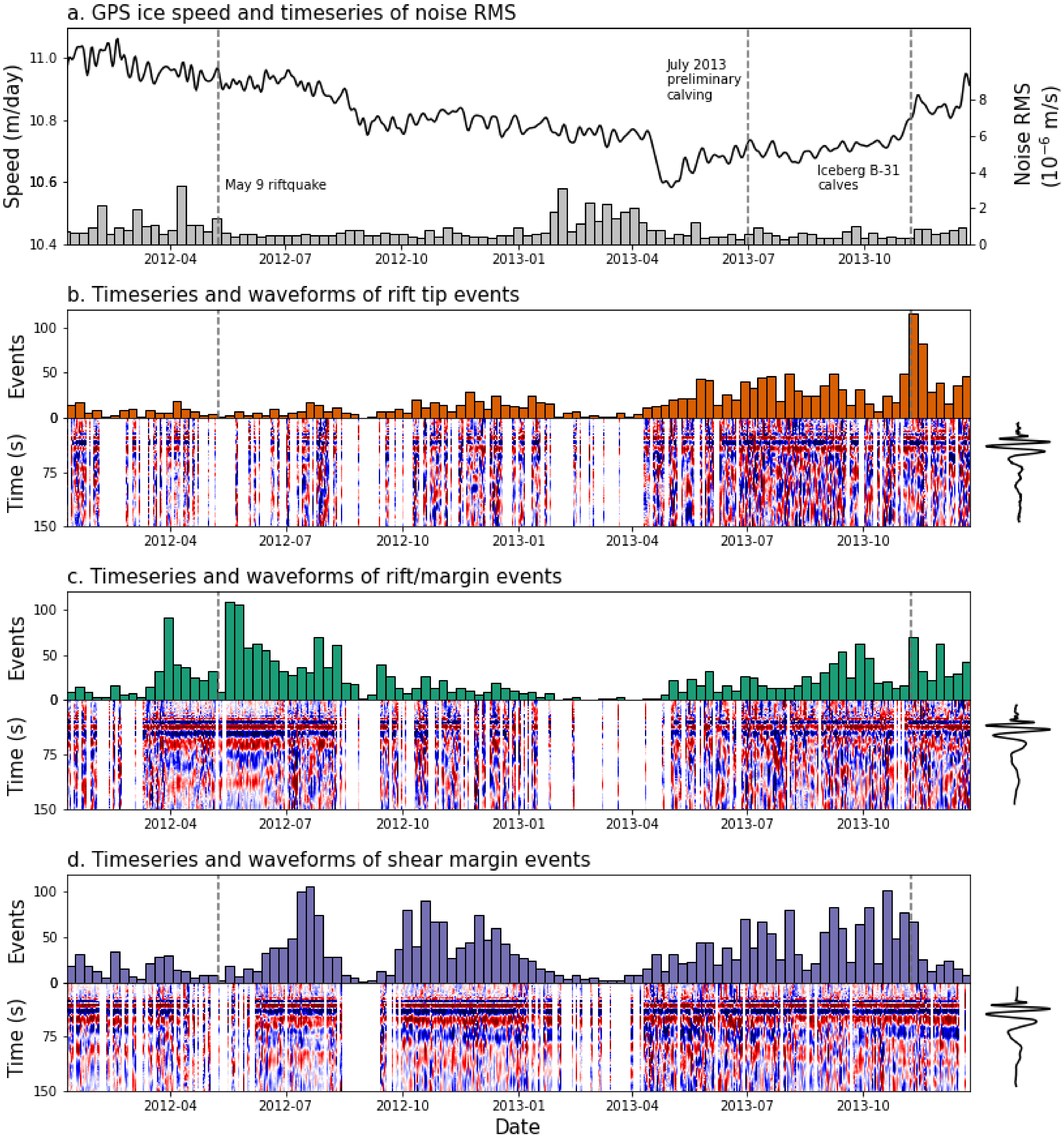

a. GPS ice speed and timeseries of noise RMS
Speed (m/day)
Noise RMS
(10^{-6} m/s)
May 9 riftquake
July 2013
preliminary
calving
Iceberg B-31
calves
b. Timeseries and waveforms of rift tip events
c. Timeseries and waveforms of rift/margin events
d. Timeseries and waveforms of shear margin events
Events
Time (s)
Date
2012-04
2012-07
2012-10
2013-01
2013-04
2013-07
2013-10

Figure 4.


a. Point moment Green's function
1e−7
Moment^{-1}seconds^{-1}
$(MPa*m*s)^{-1}$
b. Point moment source time function
Moment $(MPa*m)$
c. Point load Green's function
1e−7
Load^{-1}seconds^{-1}
$(kPa*s)^{-1}$
Time (s)
d. Point load source time function
Load (kPa)
Time (s)
*
=
e. Rift tip stack
1e−5
Displacement (m)
Time (s)

Supporting Information for "Tracking the Cracking: a Holistic Analysis of Rapid Ice Shelf Fracture Using Seismology, Geodesy, and Satellite Imagery on the Pine Island Glacier Ice Shelf, West Antarctica"

S. D. Olinger[1,2], B. Lipovsky[2], M. Denolle[2], B. Crowell[2]

[1]Department of Earth and Planetary Sciences, Harvard University, Cambridge, Massachusetts, USA

[2]Department of Earth and Space Sciences, University of Washington, Seattle, Washington, USA

Contents of this file

1. Text S1 to S4
2. Figures S1 to S8
3. Table S1

1. Text S1, GPS Processing

We processed five continuous GPS stations in the region, BOAR and SOW1-4 from 2012 to 2014. Each station was positioned kinematically in the International Terrestrial Reference Frame (ITRF) at a 30 s sample rate with GipsyX, using final Jet Propulsion Laboratory orbits. Ocean tidal loading and solid Earth tides were not removed from the derived displacement time series as these terms are needed to obtain the full glacial dynamics. After obtaining the 30 s ITRF solutions, we performed a 5 min weighted average using the inverse of the individual epoch uncertainties for data weights, and then rotated the XYZ displacements into local North, East, and up displacements.

We obtain ice speed from the processed GPS positions at the GPS station SOW3 by calculating the total distance moved in each day of the deployment and differentiating with respect to time. The resulting ice speed curve contains some spike artifacts that arise from numerical differentiation, which we remove by linearly interpolating between the ice speed before and after the affected time period. Finally, we low pass filter the data to remove trends on time periods shorter than a week.

2. Text S2, Seismogram analysis

2.1. Icequake detection

To detect flexural gravity icequakes in the dataset, we design a two-stage detection scheme that identifies broadband, dispersive seismic events. First, we employ a short term average/long term average (STA/LTA) impulsivity detector. This method identifies high-amplitude impulsive events by comparing the mean amplitude of a short time window with the mean amplitude of a long time window (Allen, 1978). The detector is triggered when STA exceeds LTA by some threshold. STA/LTA threshold values are selected by tuning the algorithm to successfully detect high signal-to-noise ratio manually-identified events (see Table S1). We carry out STA/LTA on the vertical component of each station separately in two different frequency bands (0.01-1 Hz and 1-10 Hz). Selected waveforms satisfy the STA/LTA trigger criteria in both frequency bands on at least three out of the five stations. We refine the catalog and generate waveform templates by cross-correlating each preliminary event with a master event waveform and selecting the events with cross correlation coefficients exceeding 0.9. This selection procedure resulted in 57 template events.

Second, we perform a template matching technique based on cross-correlation to identify events that were similar to the events in the preliminary catalog (Gibbons & Ringdal, 2006). To detect new events, each template event is cross correlated with all time windows in the dataset on two frequency bands (0.05-1 Hz and 1-10 Hz). We increase the lower frequency bound from 0.01 Hz to 0.05 Hz since many template events contained uninterpretable noise at frequencies below 0.05 Hz. The detector is triggered when the cross-correlation coefficient between a template event waveform and the given time window exceeds a threshold. The threshold value is selected so that the algorithm successfully detects the other known events of the preliminary catalog (see Supporting Table S1). Detected waveforms satisfy the trigger criteria on at least three out of the five stations in both frequency bands. We carry out this procedure for each template and removed redundant detections to yield the final catalog.

We detect 22,119 seismic events using the two-band template matching scheme. The detected events have a typical duration of around 50 s and an average peak vertical velocity of approximately 1e-5 m/s. Event waveforms vary in shape, indicating varied sources and propagation paths. Many of the events exhibit characteristic dispersion between 0.05 and 1 Hz with high frequencies arriving before low frequencies, while others were monochromatic between 0.05 and 1 Hz.

2.2. Waveform Clustering

Because the catalog of detected events contains both dispersive and monochromatic waveforms, we seek to cluster the events into groups based on wave shape. To do so, we modify the K-shape algorithm of Paparrizos and Gravano (2016). K-shape is designed specifically to cluster time series data. Instead of calculating the Euclidean distance between potential cluster centers and observations, K-shape calculates distances using the maximum normalized cross correlation coefficient between two time series. We adapt the K-shape algorithm for three component seismic data by independently computing the cross-correlation time series between the three separate seismic channels (vertical, East, and North). We then sum these three cross-correlation time series and calculate the distance metric as the maximum value of this summed cross correlation time series.

We use the K-shape algorithm to divide the catalog into $2, 3, \cdots, 20$ clusters. However, beyond two clusters, the differences between waveforms in each cluster become progressively less clear, and an analysis of the average distance from waveforms to their cluster center does not show significant improvement for larger numbers of clusters. We thus use the K-shape algorithm to divide the catalog into two distinct clusters, which differ based on waveform dispersion. The first cluster contains 8,184 dispersive events. The second cluster contains 13,935 monochromatic events that do not exhibit dispersion within the chosen frequency band. This difference suggests that the two types of waveforms may have been generated by different source processes. Since we are specifically interested in dispersive flexural gravity wave signals, we restrict the remaining analysis to the dispersive cluster.

3. Text S3. Methods for computing event back-azimuths.

3.1. Robust first arrival determination

We obtain the relative first arrival time of each event through phase lags measurements. We cross-correlate each respective component waveform between each seismic station. We choose a window length of 500 s around the first arrival. The trace that requires the largest shift forward in time to align with the other traces is taken to be the station of first arrival. In most cases, the first arrivals obtained independently using each component are in agreement for at least two components out of three. However, if all three components produce different stations of first arrival, a back-azimuth is not calculated and the event is disregarded.

3.2. Amplitude threshold

Next, we ensure that the polarization is extracted over a high signal to noise ratio event as against noise. We slide through the event waveform in 10 s windows with a step size of five seconds. For each 10 s time window, we check if the average amplitude of that window exceeds the average amplitude of the entire 500 s event window.

3.3. Principal component analysis

For time windows with sufficiently large amplitude, principal component analysis (PCA) is performed on the HHE (East) and HHN (North) traces from each station to retrieve the PCA components. The PCA first component is a vector whose direction explains the largest contribution of the data variance. It is equivalent to the eigenvector of the data covariance matrix that has the largest eigenvalue.

3.4. PCA first component vector correction

For waves polarized in the direction of propagation, the PCA first component vector corresponds to one of the two possible propagation directions separated by 180 degrees. Using the PCA first component vector and the geometry of the array, we compute the predicted stations of first arrival corresponding to both possible propagation directions. If the station of first arrival is in the direction of the PCA back-azimuth, the PCA first component's sign is preserved. If the station of first arrival is in the opposite direction (PCA azimuth+180 degree), we add 180 degrees to the PCA first component azimuth. This ensures that the PCA first component vector points in the direction from which incoming waves arrived.

3.5. Determining the predicted first arrival

We try three methods of computing the predicted station of first arrival corresponding to both possible propagation directions.

In the first method, we compare both possible phase back-azimuths to the back-azimuths of each station with respect to the mean station location, or array centroid. The stations that are radially closest to each possible back-azimuth are predicted to be the two possible first arrivals. The sign of the PCA first component vector is then adjusted to match the propagation direction whose predicted first arrival agree with the observed first arrival. Phases for which neither predicted first arrival agreed with the observed first arrival are discarded.

In the second method, we divide the array into two sectors along a line through the array centroid orthogonal to the PCA first component vector. The sign of the PCA first component vector is then adjusted to match the propagation direction corresponding to the sector containing the observed first arrival. No phases are discarded.

In the third method, we compute the distance vector from the array centroid to each station. For incoming plane waves, the station farthest from the array centroid in the direction of propagation records the first arrival. The stations whose distance vectors have the largest component oriented in each possible propagation directions are predicted to be the two possible first arrivals. The sign of the PCA first component vector is then adjusted to match the propagation direction whose predicted first arrival agree with the observed first arrival. Phases for which neither predicted first arrival agreed with the observed first arrival are discarded. All three methods gave relatively consistent results.

3.6. Back-azimuth stacking

Next, we sum the PCA first component vectors across each station to obtain an average vector whose norm indicates the level of agreement between propagation directions calculated at each station. Finally, we take the arctangent of the quotient of the two elements of the PCA component vector to retrieve a back-azimuth. Because this procedure is repeated for each 10 s time window in the event, the result for each individual event is a distribution of back-azimuths calculated for each time window within that event.

To obtain a single back-azimuth for each event, we take the average of the back-azimuths calculated using each time window in the data. We use the mean of circular quantities, with the back-azimuth from each time window weighted by the norm of the summed PCA components across the array for that window. This means that time windows with poor agreement between stations are downweighted when taking the average back-azimuth. The weighted mean of circular quantities is expressed below for the back-azimuth distribution $\theta_1, ..., \theta_n$ with PCA norms $w_1, ..., w_n$ of an event with n time windows:

$$\bar{\theta} = \text{atan2}\left(\frac{1}{n}\sum_{j=1}^{n} w_j \sin(\theta_j), \frac{1}{n}\sum_{j=1}^{n} w_j \cos(\theta_j)\right) \tag{1}$$

4. Text S4, Flexural gravity wave model

4.1. Analytical Solution for Ocean Surface Waves

We examine the water velocity potential function ϕ and relate it to the vertical ice shelf velocity w. We first solve the ocean surface wave equation for a body of water with infinite length and finite depth:

$$\frac{\partial^2 \phi}{\partial x^2} + \frac{\partial^2 \phi}{\partial y^2} = 0 \tag{2}$$

over the interval $-\infty < x < \infty, -h_w < y < 0$. We enforce zero velocity at the ocean floor and couple vertical velocity to the rate of beam deflection at the ocean surface:

$$\frac{\partial \phi}{\partial y}\Big|_{y=-h_w} = 0 \frac{\partial \phi}{\partial y}\Big|_{y=0} = \frac{\partial w}{\partial t} \tag{3}$$

We enforce the Sommerfeld radiation condition:

$$\phi\Big|_{x\to-\infty} = \frac{\partial \phi}{\partial x}\Big|_{x\to-\infty} = 0 \tag{4}$$

$$\phi\Big|_{x\to\infty} = \frac{\partial \phi}{\partial x}\Big|_{x\to\infty} = 0 \tag{5}$$

We apply the Fourier Transform, written for an arbitrary function $f(x)$ as

$$\bar{f}(k) = \int_{-\infty}^{\infty} f(x) e^{-i\xi x} dx \tag{6}$$

The time-wavenumber domain solution that satisfies the governing equation and boundary conditions is,

$$\bar{\phi} = \frac{\partial \bar{w}}{\partial t}\left(\frac{\cosh(\xi(h_w + y))}{\xi \sinh(h_w \xi)}\right). \tag{7}$$

We note that ϕ is a linear function of w, therefore permitting us to write the floating beam equation using the linear operator $\mathcal{A}$ as noted in the main text.

4.2. Analytic Solution for Buoyant Ice Shelf Flexure

To interrogate the source process that explains the observations, we obtain the Green's function, or fundamental solution of a floating dynamic beam to an impulse forcing. We obtained the Green's function by using integral transform methods to solve the governing equation for an impulse forcing in space and time. We write the Green's function formulation of (2):

$$\rho_i h_i \frac{\partial^2 G}{\partial t^2} + D\frac{\partial^4 G}{\partial x^4} + \rho_w g G + \rho_w \frac{\partial \phi}{\partial t} = \delta(x)\delta(t) \tag{8}$$

where G is the Green's function, $\delta(x)$ is Dirac delta function in space, and $\delta(t)$ is the Dirac delta function in time. As before, we apply the Fourier Transform in space to each term. Next, we apply the Laplace transform, defined as,

$$g^*(s) = \int_0^\infty g(t)e^{-st}dt$$

We can then solve for $\bar{G}^*$ algebraically:

$$\bar{G}^* = \frac{\frac{1}{\rho_i h_i + \rho_w \gamma}}{\frac{D\xi^4 + \rho_w g}{\rho_i h_i + \rho_w \gamma} + s^2} \tag{9}$$

Finally, we analytically compute the inverse Laplace transform of Equation 9 to obtain the Fourier-transformed Green's function,

$$\bar{G}(k,t) = \frac{\sin\left(t\sqrt{\frac{D\xi^4+\rho_w g}{\rho_i h_i+\rho_w\gamma}}\right)}{\sqrt{\rho_i h_i + \rho_w \gamma}\sqrt{D\xi^4 + \rho_w g}} \tag{10}$$

In practice, we numerically calculate $\bar{G}$ for a range of times and wavenumbers that define the temporal and spatial domain of the model run. Once $\bar{G}$ is calculated for each element of a vector of times and a vector of wavenumbers, the IFFT (inverse fast Fourier transform) is taken to numerically retrieve the Green's function $G(x,t)$ of the ice shelf for an applied unit point force.

4.3. Greens function for a point moment source

To retrieve the impulse response to a point bending moment source, we note that an applied bending moment is equivalent to a pair of infinitesimally-spaced point loads with opposite signs:

$$G_m(x,t) = [G(x,t) - G(x+\Delta x,t)]_{\Delta x \to 0}$$

$$G(x,t) = \Delta x \left[\frac{G(x,t) - G(x+\Delta x,t)}{\Delta x}\right]_{\Delta x \to 0}$$

$$G(x,t) = \frac{dG(x,t)}{dx}$$

To obtain $G_m(x,t)$, we numerically take the spatial derivative of the point load Green's function $G(x,t)$.

4.4. Deconvolution procedure

We calculate source load through the deconvolution,

$$P_{\text{estimated}}(t) = \mathcal{F}^{-1}\left[\frac{\hat{w}(\omega)_{\text{observed}}}{\hat{G}(x_0,\omega)}\right], \tag{11}$$

Table S1. Parameters for building the event catalog.

Parameter	Low Frequency Band	High Frequency Band
STA/LTA band	0.01-1 Hz	1-10 Hz
Short window (ST) length	10 s	10 s
Long window (LT) length	300 s	300 s
Trigger STA/LTA threshold	8 s	20 s
Template matching band	0.05-1 Hz	1-10 Hz
Trigger cross correlation threshold	0.3	0.2
Minimum number of stations for a detection	3	3

where hats denote Fourier-transformed quantities, $\mathcal{F}^{-1}$ is the inverse Fourier transform, $w_{\text{observed}}(t)$ is a linear stack of observed displacement seismograms, $P_{\text{estimated}}(t)$ is an estimated source load distribution, and x_0 is the station epicentral distance. We obtain $w_{\text{observed}}(t)$ for each spatial group by aligning each waveform in the group with respect to a master event using cross correlation and taking the average waveform. Master events were selecting by finding the event from each spatial group that was best-correlated with the overall centroid of the dispersive cluster. We choose x_0 corresponding to the average distance to each spatial group: for the rift tip, $x_0 = 25$ km; for rift/margin, $x_0 = 25$ km; for margin icequakes, $x_0 = 17.5$ km. We alternatively consider a bending moment source through the relationship,

$$M_{\text{estimated}}(t) = \mathcal{F}^{-1}\left[\frac{w(\omega)_{\text{observed}}}{G_m(x_0,\omega)}\right]. \tag{12}$$

Table S1.

References

Allen, R. V. (1978, 10). Automatic earthquake recognition and timing from single traces. *Bulletin of the Seismological Society of America*, *68*(5), 1521-1532. Retrieved from `https://doi.org/10.1785/BSSA0680051521` doi: 10.1785/BSSA0680051521

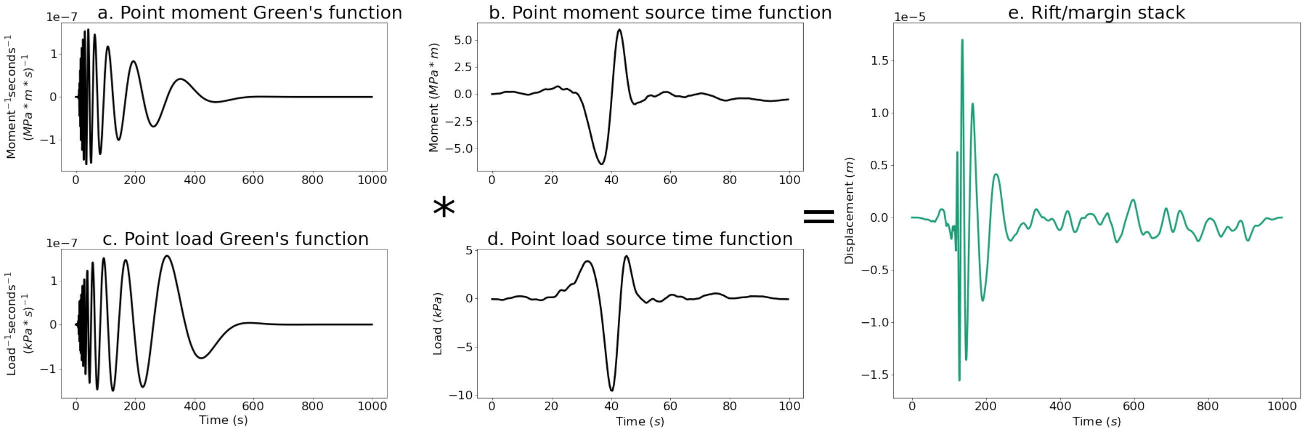

Figure S1. Green's functions and source time functions for rift/margin events. (a) Theoretical Green's function for a bending moment source located at a distance of 30 km, which is approximately the distance from PIG seismic array to the rift/margin area. (b) Source time function retrieved by deconvolving the moment Green's function from the stack of rift/margin vertical displacement waveforms. (c) Theoretical Green's function for a point load source located at a distance of 30 km, which is approximately the distance from PIG seismic array to the rift/margin area. (d) Source time function retrieved by deconvolving the point load Green's function from the stack of rift/margin vertical displacement waveforms. (e) Stack of rift/margin vertical displacement waveforms obtained by aligning waveforms to a master event and taking the mean waveform on the frequency band 0.01-1 Hz.

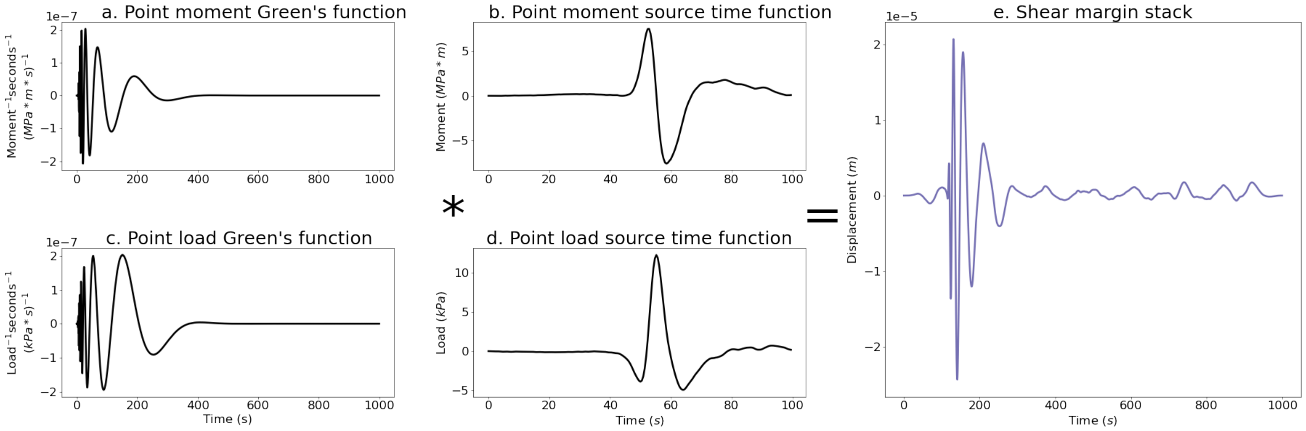

Figure S2. Green's functions and source time functions for shear margin events. (a) Theoretical Green's function for a bending moment source located at a distance of 17.5 km, which is approximately the distance from PIG seismic array to the northeast shear margin near Evans Knoll. (b) Source time function retrieved by deconvolving the moment Green's function from the stack of shear margin vertical displacement waveforms. (c) Theoretical Green's function for a point load source located at a distance of 17.5 km, which is approximately the distance from PIG seismic array to the shear margin. (d) Source time function retrieved by deconvolving the point load Green's function from the stack of shear margin vertical displacement waveforms. (e) Stack of shear margin vertical displacement waveforms obtained by aligning waveforms to a master event and taking the mean waveform on the frequency band 0.01-1 Hz.

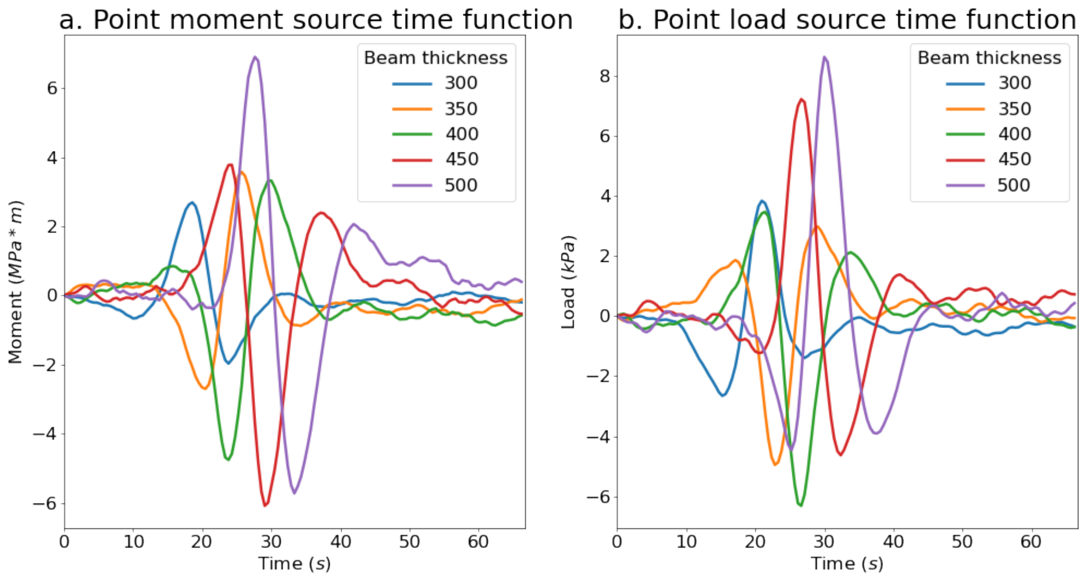

Figure S3. Sensitivity of rift tip source time function deconvolution to modeled ice thickness. Modeled beam thicknesses are shown in the legend. Source time functions generally have larger amplitude and longer duration for thicker beams, because larger forcing is required to induce a given displacement for a more rigid beam. Flexural rigidity, the parameter that governs flexure, is a function of thickness.

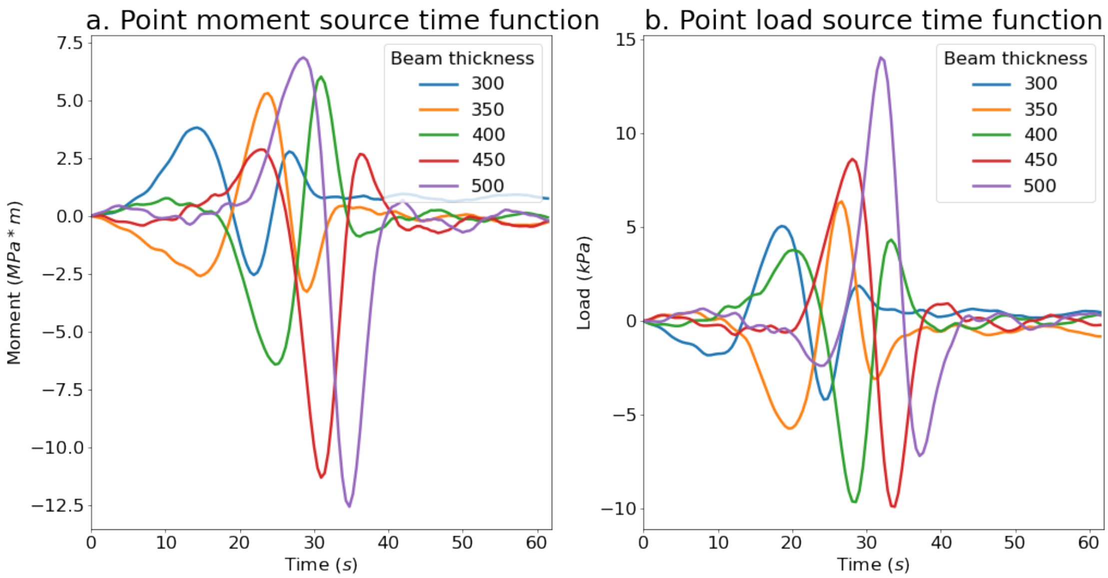

Figure S4. Sensitivity of rift/margin source time function deconvolution to modeled ice thickness. Modeled beam thicknesses are shown in the legend. Source time functions generally have larger amplitude and longer duration for thicker beams, because larger forcing is required to induce a given displacement for a more rigid beam. Flexural rigidity, the parameter that governs flexure, is a function of thickness.

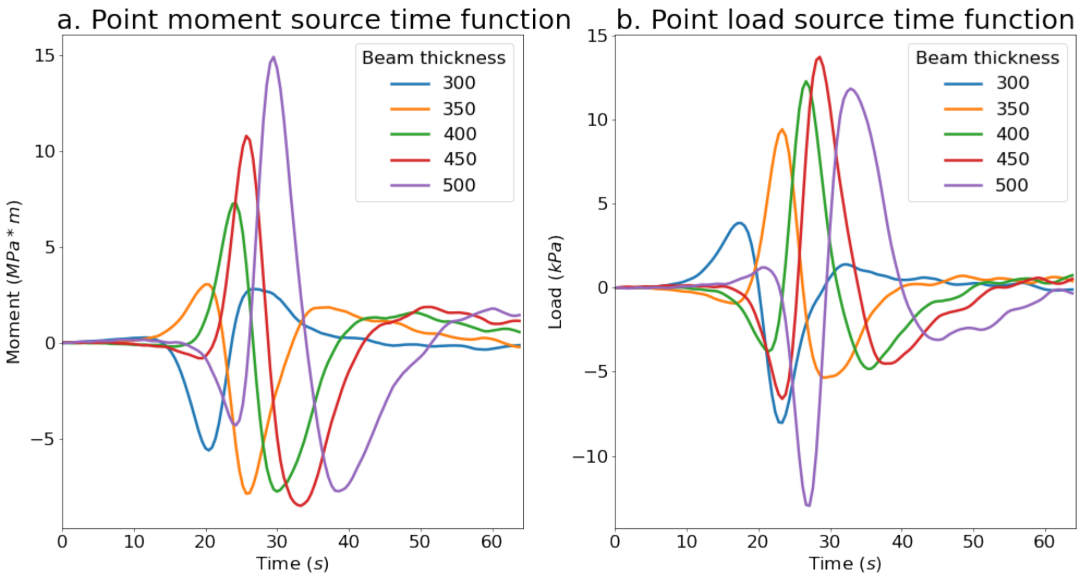

Figure S5. Sensitivity of margin source time function deconvolution to modeled ice thickness. Modeled beam thicknesses are shown in the legend. Source time functions generally have larger amplitude and longer duration for thicker beams, because larger forcing is required to induce a given displacement for a more rigid beam. Flexural rigidity, the parameter that governs flexure, is a function of thickness.

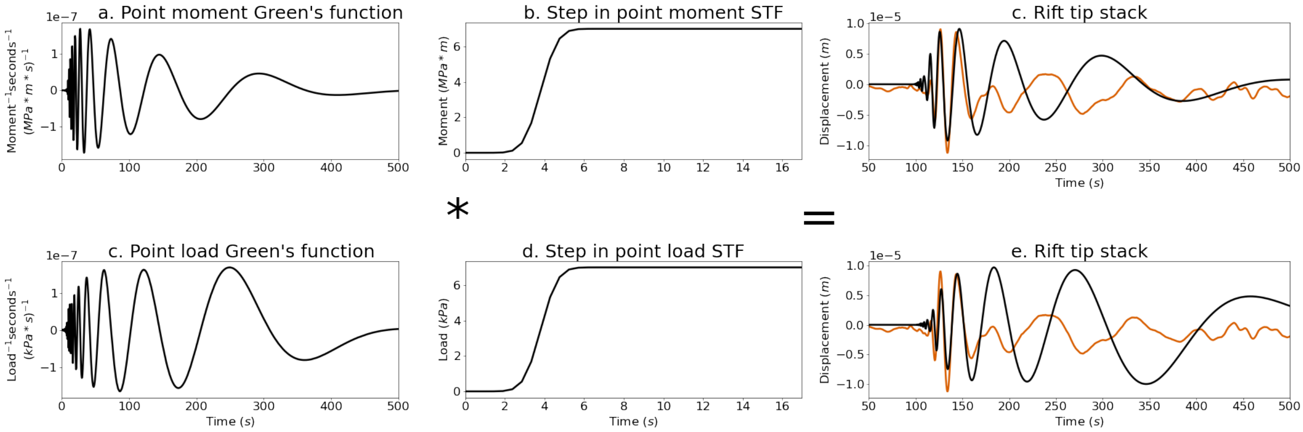

Figure S6. Modeled rift tip Green's function convolved with step source time function. The resulting modeled displacements, shown in black, have a longer decay and larger amplitdue low-frequency displacements than the rift tip stack, shown in orange, for both bending moment and point load sources.

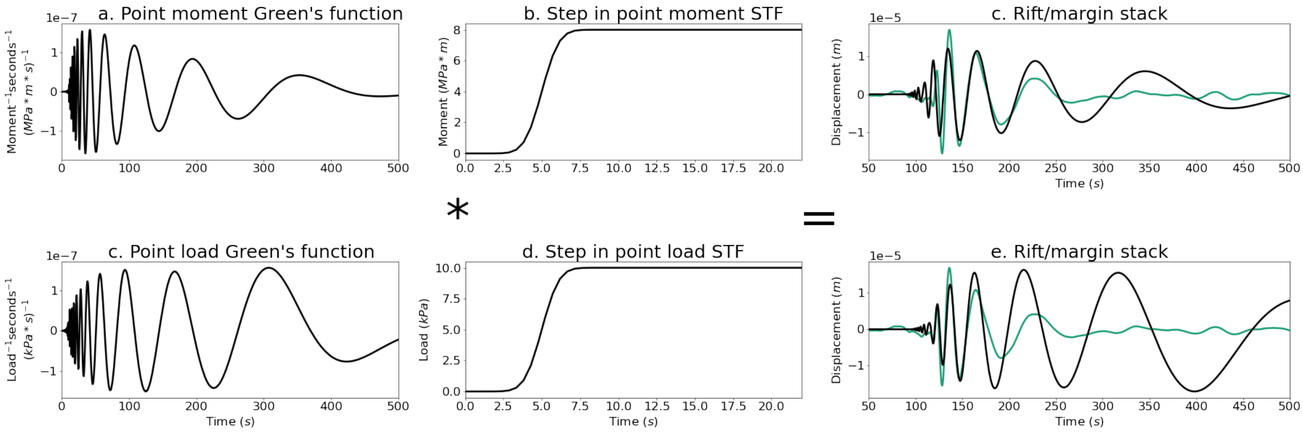

Figure S7. Modeled rift/margin Green's function convolved with step source time function. The resulting modeled displacements, shown in black, have a longer decay and larger amplitdue low-frequency displacements than the rift/margin stack, shown in green, for both bending moment and point load sources.

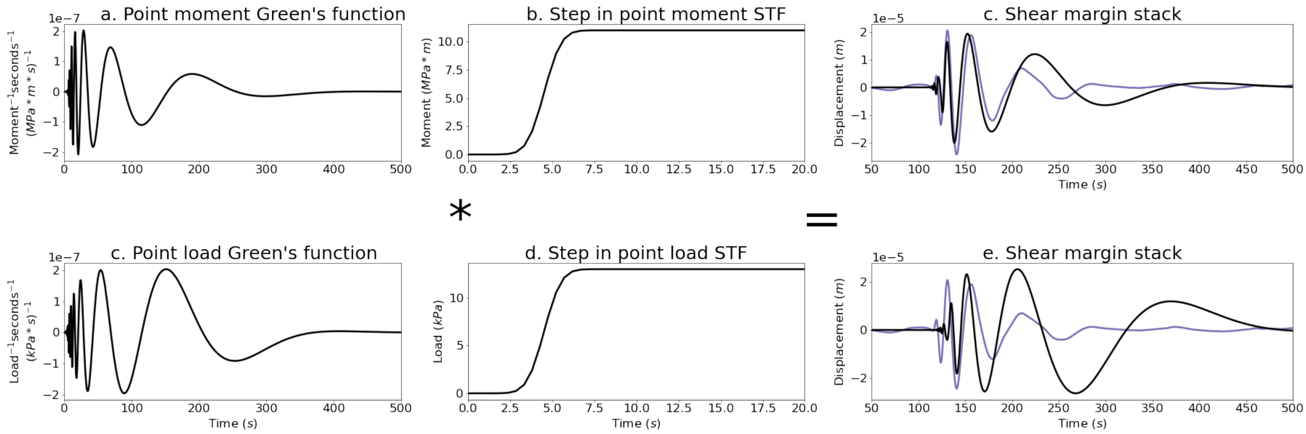

Figure S8. Modeled shear margin Green's function convolved with step source time function. The resulting modeled displacements, shown in black, have a longer decay and larger amplitdue low-frequency displacements than the shear margin stack, shown in purple, for both bending moment and point load sources. The modeled displacements arising from an applied bending moment are relatively similar to the shear margin stack, but the results of deconvolution do not support the hypothesis that the observations were generated by a step forcing in bending moment.

Gibbons, S. J., & Ringdal, F. (2006, 04). The detection of low magnitude seismic events using array-based waveform correlation. *Geophysical Journal International*, *165*(1), 149-166. Retrieved from https://doi.org/10.1111/j.1365-246X.2006.02865.x doi: 10.1111/j.1365-246X.2006.02865.x

Paparrizos, J., & Gravano, L. (2016, June). K-shape: Efficient and accurate clustering of time series. *SIGMOD Rec.*, *45*(1), 69–76. Retrieved from https://doi.org/10.1145/2949741.2949758 doi: 10.1145/2949741.2949758